An Implicit Energy- and Charge-conserving Electromagnetic PIC algorithm for Paraxial Magnetic Nozzles

IEPC-2024-378

Presented at the 38th International Electric Propulsion Conference, Toulouse, France
June 23-28, 2024

Pedro Jiménez* and Mario Merino,
Aerospace Engineering Department, Universidad Carlos III de Madrid, Leganés, Madrid, Spain

and

Luis Chacón
Los Alamos National Laboratory, Los Alamos, NM, USA.

We present a Darwin-electromagnetic, 1D3V time-implicit, energy- and charge- conserving Particle-in-Cell (PIC) algorithm, and its application to the study of electrodeless plasma thrusters with magnetic nozzles. A fully ionized, collisionless plasma composed of singly charged ions and electrons is injected into a paraxial, convergent-divergent magnetic field topology, and a right-hand polarized wave is fed through the upstream boundary. The electromagnetic simulation results are compared with a cold-plasma wave and electrostatic (i.e. no-wave) simulations. Wave heating increases the electron perpendicular temperature, especially in the vicinity of the electron cyclotron resonance. The energized electrons drive a more pronounced potential drop and a higher ion acceleration than in the absence of waves. Kinetic features, such as the Doppler broadening of the ECR heating region, are detected in the electron velocity distribution function. The linear, prescribed cold-plasma and nonlinear, self-consistent kinetic results for the wave fields are similar once the reduced model phenomenological collisionality is adjusted. Computational scaling estimates show that the time-implicit PIC algorithm may facilitate realistic electromagnetic kinetic simulations of plasma thrusters in one or more dimensions, which were previously too costly.

I. Introduction

Electrodeless Plasma Thrusters (EPTs) are a class of electric propulsion devices that do not require hollow cathodes for ion beam neutralization, promising simplified power processing units, enhanced lifetimes, and the flexibility to use alternative propellants. Among the various EPT designs, the Helicon Plasma Thruster (HPT) [1, 2, 3] and the Electron Cyclotron Resonance Thruster (ECRT) [4, 5, 6] have gained much of the community attention in the past decade. A key feature of these thrusters is the utilization of electromagnetic waves to energize the charged particles, along with a downstream plasma expansion into vacuum guided by a magnetic nozzle (MN). They differ in their geometrical details, operating frequencies (in the MHz and low GHz ranges, respectively), and power coupling mechanisms. Understanding the physics of the discharge and acceleration and, in particular, the plasma-wave interaction is a significant challenge in the optimization of these devices.

The complex interaction between a plasma and electromagnetic waves in EPTs has previously been modeled using simplified linearized cold-plasma models in the frequency domain, sometimes coupled with plasma transport solvers [7, 8]. However, traditional simulation approaches fail to capture nonlinear effects

*pejimene@ing.uc3m.es.

and kinetic phenomena. To overcome these limitations, self-consistent kinetic-electromagnetic simulations are required. Due to the high computational cost, such simulations are scarce. One of those few examples is the recent work by Porto et al. [9]. The study employs 1D explicit particle-in-cell/Maxwell simulations with a Constrained Interpolation Profile (CIP) scheme to model transverse fields propagating through a plasma in a magnetic nozzle. The results show anisotropic plasma heating inside the coaxial chamber and a trapped population of electrons with higher perpendicular energy in the plume. The CIP method alleviates the CFL condition for fast wave propagating modes, but it does not eliminate the need to solve quite short time and length scales.

Although electromagnetic kinetic simulations are rare in the literature, electrostatic particle-in-cell (PIC) codes are common in the simulation of plasma physics inside thrusters and their plumes [10, 11, 12, 13]. The vast majority of these studies employ the time-explicit leapfrog scheme [14]. Explicit PIC codes suffer from timestep and cell-size constraints, requiring resolution of the electron plasma frequency and the Debye length for stability. As such, their computational demands are huge and their application is limited to small domains or to problems with modified vacuum permittivity ε_0. Moreover, some explicit PIC formulations are momentum-conserving but lack strict energy conservation, which is advisable for e.g. instability analysis.

Time-implicit energy- and charge-conserving PIC algorithms [15], and also semi-implicit ones [16], are being proposed as a powerful tool to overcome these limitations and conduct realistic simulations with reasonable computational resources. Indeed, the implicit time-stepping allows bypassing the plasma frequency constraint, damping those (generally uninteresting) electrostatic oscillations if desired. Similarly, the formulation enables us to use cell sizes larger than the Debye length without incurring finite grid instabilities. Remarkably, this substantial reduction in computational costs comes without sacrificing accuracy. Implicit PIC codes are recently being developeda and applied in various research fields, including nuclear fusion [17] and material processing [18]. Their application to electric propulsion studies has been relatively unexplored until recently [19, 7]. These algorithms were initially developed for electrostatic scenarios [15], but recent studies in one and multiple dimensions [20, 21] have shown that incorporating the electromagnetic (EM) Darwin approximation [22, 23], which excludes light-speed traveling modes, implicit PIC methods enable efficient and accurate kinetic electromagnetic simulations over long time periods.

Building on a recently published electrostatic 1D-1V investigation of the plasma expansion in an MN [7], this work addresses the electromagnetic, 1D-3V simulation of a MN with an applied right-hand polarized wave, in a configuration representative of ECRTs (but also HPTs, where it has been shown that a downstream ECR surface exists in the nozzle where the energy absorption per particle is not negligible [24]). This is achieved by extending our time-implicit PIC model with an electromagnetic Darwin model. New boundary conditions for EM wave fields are also introduced. Preliminary plasma profiles including potential, density, and temperature are presented. Electron heating by EM waves results in a more pronounce potential drop that accelerates ions to faster velocities. We also explore the wave effects in the electron velocity distribution function (EVDF) with several phase space plots. Inherently kinetic phenomena such as Doppler-shifted ECR heating are observed in these results. The PIC-Darwin results are compared with (1) electrostatic results which do not include wave propagation nor heating, and (2) a simulation that imposes the wave fields that would result from the linear cold-plasma approximation, instead of the self-consistent EM fields. We find that the cold-plasma wavefields are a good approximation of the self-consistent ones once the effective damping parameter in that model is tuned to reproduce the resonance broadening. This is a key finding that exemplifies how kinetic simulations can be used to fit faster, simpler simulation models. We discuss that the implicit electromagnetic PIC approach can achieve significant computational savings while maintaining accuracy and conservation properties.

The remainder of the paper is organized as follows. Section II introduces the 1D-3V electromagnetic model, including the particle and field equations and their numerical discretization in the implicit PIC algorithm. A verification case with periodic boundary conditions can be found in Appendix A at the end of the text, showcasing the advertised conservation of global energy and local charge and the accurate reproduction of analytical growth rates for the electron Weibel instability. Section III presents the new EM PIC magnetic nozzle simulations and compares the self-consistent Darwin simulations with the previous electrostatic results and the wave fields derived from the cold-plasma model presented in Section III.A.1. Finally, conclusions are drawn, and future work is proposed in Section IV.

II. Methodology

We study the collisionless plasma expansion in an axisymmetric, convergent-divergent, applied magnetic field $\boldsymbol{B}_0$. The plasma is composed of warm electrons e and single-charge ions i. Our region of interest is the neighborhood of the axis of the resulting MN, which is aligned with the z direction of the Cartesian $\{\mathbf{1_z}, \mathbf{1_x}, \mathbf{1_y}\}$ vector basis. In the paraxial approximation, the applied magnetic field is assumed to change slowly over lengths comparable to the characteristic radial gradient length of plasma properties R,

$$R\frac{\partial \ln B_{z0}}{\partial z} = \varepsilon \ll 1. \tag{1}$$

The divergenceless nature of $\boldsymbol{B}_0$ means that, in the neighborhood of the axis and to order ε, the radial magnetic field is

$$B_{r0} = -\frac{r}{2}\frac{\partial B_{z0}}{\partial z}. \tag{2}$$

We shall further assume that the Larmor radius of all particles is small compared to that radial length,

$$\frac{\ell_s}{R} \leq O(\varepsilon), \quad s = i, e. \tag{3}$$

Then, at the centerline of the MN and over distances comparable to ℓ_s, the variation of any other fields and particle distributions in the radial direction is of order $O(\varepsilon^2)$. This means that fields and distributions can be taken as radially uniform to order $O(\varepsilon)$ within the trajectories of the particles.

Finally, to maintain the solenoidal property of the magnetic field [25], we incorporate the paraxial factor $J^B(z) = 1/B_{z0}(z)$ into the divergence operator, ensuring:

$$\nabla \cdot \boldsymbol{B}_0 = \frac{1}{J^B}\frac{\partial}{\partial z}\left(J^B B_{z0}\right) = 0. \tag{4}$$

By conservation of the magnetic flux, this factor is proportional to the flux tube area A_t at each nozzle cross-section $A_t(z)B(z) =$ constant. The characteristic frequencies for the problem dynamics are the plasma frequency, which is proportional to the square root of the density $\omega_{pe} = \sqrt{n_e q_e^2/\varepsilon_0 m_e}$ and the cyclotron frequency, proportional to the magnetic field strength $\omega_{ce} = eB_{z0}/m_e$. In general, we will have $\omega_{pe} \gg \omega_{ce} \sim \omega$, where ω is the frequency of the injected electromagnetic waves fed through the upstream boundary.

A. Particle evolution equations

The Vlasov equation describes the evolution of each plasma species distribution function f_s $(s = i, e)$ in the collisionless limit,

$$\frac{\partial f_s}{\partial t} + \boldsymbol{v}\cdot\nabla_{\boldsymbol{x}} f_s + \frac{q_s}{m_s}\left(\boldsymbol{E} + \boldsymbol{v}\times(\boldsymbol{B}+\boldsymbol{B}_0)\right)\cdot\nabla_{\boldsymbol{v}} f_s = 0, \tag{5}$$

where we have used $\boldsymbol{E}$ and $\boldsymbol{B}$ to indicate the variable electric and magnetic fields, and $\boldsymbol{B}_0$ for the steady, applied magnetic field of the MN. Upon discretizing the 1D3V distribution function into macroparticles with Cartesian velocity coordinates, we get:

$$f_s(z, v_z, v_x, v_y, t) = \sum_{p\in s} w_p \delta\left(z - z_p(t)\right)\delta\left(v_z - v_{zp}(t)\right)\delta\left(v_x - v_{xp}(t)\right)\delta\left(v_y - v_{yp}(t)\right). \tag{6}$$

where $\delta(x)$ denotes the Dirac delta function, and the subindex p runs over all macroparticles. Introducing (6) into (5) we get the following particle evolution equations:

$$\begin{aligned}
&\frac{\mathrm{d}w_p}{\mathrm{d}t} = 0,\\
&\frac{\mathrm{d}z_p}{\mathrm{d}t} = v_{z,p},\\
&\frac{\mathrm{d}v_{z,p}}{\mathrm{d}t} = \frac{q_s}{m_s}\left(E_z + v_{xp}B_y - v_y B_x\right) - \frac{1}{2B_{z0}}\frac{\partial B_{z0}}{\partial z}\left(v_{xp}^2 + v_{yp}^2\right),\\
&\frac{\mathrm{d}v_{xp}}{\mathrm{d}t} = \frac{q_s}{m_s}\left(E_x + v_{yp}B_{z0} - v_{zp}B_y\right) + \frac{1}{2B_{z0}}\frac{\partial B_{z0}}{\partial z}v_{zp}v_{xp},\\
&\frac{\mathrm{d}v_{yp}}{\mathrm{d}t} = \frac{q_s}{m_s}\left(E_y - v_{xp}B_{z0} + v_{zp}B_x\right) + \frac{1}{2B_{z0}}\frac{\partial B_{z0}}{\partial z}v_{zp}v_{yp}.
\end{aligned} \tag{7}$$

The 38th International Electric Propulsion Conference, P. Baudis Convention Center, Toulouse, France, June 23-28, 2024

The last term in the each velocity evolution equation represents the magnetic mirror force on the macroparticle.

The macroparticles are injected through the upstream boundary of the domain. The sampling of both electrons and ions is carried out from a semi-Maxwellian flux with injection densities n_e^* and n_i^*, refer to [7] for details of the injection routines. A key aspect of the code that allows obtaining simulation results without spurious sheaths at the upstream or downstream boundaries is the choice of boundary conditions at both ends: upstream, the number of electrons injected is dynamically modified by an heuristic control law, while the injection density of ions n_i^* is kept constant. Downstream, the least energetic electrons are reflected back into the domain, depending on a dynamically-computed threshold energy [26]. This combination of physically-consistent boundary conditions yields an essentially-quasineutral plasma expansion everywhere.

B. Electromagnetic field equations

To characterize the electromagnetic fields, we introduce the scalar ϕ and vector $\boldsymbol{A}$ potentials,

$$\begin{aligned} \boldsymbol{E} &= -\nabla\phi - \frac{\partial \boldsymbol{A}}{\partial t}, \\ \boldsymbol{B} &= \nabla \times \boldsymbol{A}. \end{aligned} \tag{8}$$

Furthermore, we choose to impose the Coulomb gauge, $\nabla \cdot \boldsymbol{A} = 0$. Note that in this 1D description (with $\partial_x = \partial_y = 0$), the Coulomb gauge requires $\partial A_z/\partial z = 0$. Moreover, $A_z(z)$ does not contribute to $\boldsymbol{B}$, while any arbitrary $\boldsymbol{E}_z$ can be modeled through ϕ alone. Hence, and without loss of generality, we take $A_z = 0$.

To obtain the equation for the electrostatic potential $\phi(z)$, we follow [15] and consider Ampère's law,

$$\varepsilon_0 \frac{\partial \boldsymbol{E}}{\partial t} + \boldsymbol{j} = \frac{1}{\mu_0} \nabla \times \mathbf{B}. \tag{9}$$

Taking the divergence of this equation eliminates the curl of the magnetic field, yielding:

$$\varepsilon_0 \frac{\partial}{\partial t} \nabla^2 \phi = \nabla \cdot \mathbf{j} \quad \Rightarrow \quad \varepsilon_0 \frac{\partial}{\partial t} \frac{\partial}{\partial z} \left(J^B \frac{\partial \phi}{\partial z} \right) = \frac{\partial (J^B j_z)}{\partial z}. \tag{10}$$

This equation is equivalent to the time derivative of Poisson's equation, when charge conservation $\partial_t \rho = -\nabla \cdot \boldsymbol{j}$ is taken into account. Numerically, and because of the strict charge conservation property of the algorithm, integrating Poisson's equation or (10) yield identical results.

The boundary conditions for the electrostatic potential ϕ are the same as in [7]. The upstream potential is fixed to a reference value (Dirichlet BC); downstream, the following Neumann condition on ϕ is imposed, arising from integrating equation(10) in z

$$\varepsilon_0 \frac{\partial}{\partial t} \frac{\partial}{\partial z} \phi - j_z = C(t) B(z). \tag{11}$$

where the integration constant $C(t)$ can only depend on time, and the factor $B(z)$ comes from integrating in a flux tube of varying cross sectional area. Approaching steady-state, time derivatives of ϕ go to zero, and in the case of a current-free magnetic nozzle, $j_z = 0$. Hence, we fix $C(t) = 0$ for all t, and use equation (11) to solve for $\partial\phi/\partial z$ as a function of j_z at the boundary [7].

To find the equation for the vector potential $\boldsymbol{A} = A_x \mathbf{1}_x + A_y \mathbf{1}_y$, we come back to Ampère's equation (9) to obtain:

$$-\varepsilon_0 \left(\frac{\partial \nabla \phi}{\partial t} + \frac{\partial^2 \boldsymbol{A}}{\partial t^2} \right) + \boldsymbol{j} = -\frac{1}{\mu_0} \nabla^2 \boldsymbol{A}. \tag{12}$$

The Darwin approximation to Maxwell's equations is a simplification used in the study of quasistatic electromagnetic fields, particularly in scenarios where the effects of electromagnetic radiation can be neglected compared to sources, such as plasma currents [27]. This approximation is applicable in systems where the variations in the fields are slow enough so that part of the displacement current can be considered negligible. The approximation is derived by neglecting the term on $\partial^2 \boldsymbol{A}/\partial t^2$ [23]. The final equations for A_x and A_y are then:

$$\frac{\partial}{\partial z} \left(J^B \frac{\partial A_x}{\partial z} \right) = -\mu_0 J^B j_x, \tag{13}$$

$$\frac{\partial}{\partial z} \left(J^B \frac{\partial A_y}{\partial z} \right) = -\mu_0 J^B j_y. \tag{14}$$

Regarding the boundary conditions for $\boldsymbol{A}$, time-varying Dirichlet conditions for a right-hand polarized wave at a frequency ω at the upstream boundary are imposed. At the downstream boundary, we set $A_{x,n_z} = A_{y,n_z} = 0$. This is justified by having an upstream electron cyclotron surface that absorbs the incoming electromagnetic power as shown in Section III. In fact, simulation results confirm that the $\boldsymbol{A}$ potential reaching the downstream end is near zero and that reflection is negligible.

C. Numerical implementation

Next we summarize the discretization of the field and particle equations presented in the last section. The present implementation of the model can work with analytical mesh maps $z(\xi)$, where ξ is the coordinate in logical space [28]. These are used to accommodate non-uniform meshes that can accurately resolve field gradients and maintain a good balance of macroparticles per cell with a reduced number of total cells. This is accomplished by the introduction of the map Jabobian $\partial_\xi z$ into the field equations. The particle mover equations must also account for the mesh map through a hybrid mover strategy that advances velocities in physical space and positions in logical space. For simplicity, we have not expanded in ξ the neither the continuous nor the discrete equations; refer to [7, 28] for details. Following [29] and [7], a segment-averaged weighting strategy is introduced that allows particles to cross several cells within a single suborbit providing additional gains in computational performance. Again, the necessary modifications to the weighting equations are skipped for simplicity in this model section, but can be found in [7].

In the following, the cell faces are identified with semiinteger indexes $(i + 1/2)$ and the cell centers with integer indexes (i). For simplicity, we consider a uniform mesh with n_z cells at Δz intervals, although, as mentioned earlier, the algorithm can also employ nonuniform grids via a mesh map $z(\xi)$. Figure 1 sketches the discrete space-time positions used in the simulation. Potentials are discretized at cell centers and at integer timesteps. Currents are computed at semiinteger timesteps, the axial one at cell faces while the transversal components are saved at cell centers. The electromagnetic field computation is performed with second-order-centered finite differences (in time or space) from the corresponding potentials according to (8). The operator $\partial^2/\partial z^2$ appearing in (10) and (12) is discretized as $(f_{i+1} - 2f_i + f_{i-1})/\Delta z^2$ to be consistent with the repeated application of the discrete version of $\partial/\partial z$ [30].

The particle evolution equations (7) are integrated with a second-order time-centered Crank-Nicolson implicit scheme similar to [30]. Particle orbits are solved in one or several suborbits. Instead of using the full time step Δt, varying substeps $\Delta\tau_p^\nu$ are used for each suborbit ν, chosen so that $\sum \Delta\tau_p^\nu = \Delta t$. This method relies on the difference in scales between the slow field dynamics, represented by Δt, and the rapid particle dynamics, represented by $\Delta\tau$. The substep is controlled by an error estimator [7] and might be different for each particle in the simulation. By doing so, we ensure accurate orbit integration while minimizing memory access, as particle coordinates are stored in local registers during subsequent suborbits.

The scattering of the electric fields to particle positions is consistent with the weighting of the current components to ensure exact global energy conservation [30] (not proven here):

$$
\begin{aligned}
E_{z,p}^{\nu+1/2} &= \sum_i \frac{E_{z,i+1/2}^{n+1} + E_{z,i+1/2}^{n}}{2} S_1\left(z_p^{\nu+1/2} - z_{i+1/2}\right), \\
E_{x,p}^{\nu+1/2} &= -\sum_i \frac{A_{x,i}^{n+1} - A_{x,i}^{n}}{\Delta t} S_2\left(z_p^{\nu+1/2} - z_i\right), \\
E_{y,p}^{\nu+1/2} &= -\sum_i \frac{A_{y,i}^{n+1} - A_{y,i}^{n}}{\Delta t} S_2\left(z_p^{\nu+1/2} - z_i\right), \\
J^B j_{z,i+1/2}^{n+1/2} &= \frac{1}{\Delta t \Delta z} \sum_p \sum_\nu q_p v_{p,z}^{v+1/2} S_1\left(z_p^{\nu+1/2} - z_{i+1/2}\right) \Delta\tau_p^\nu, \\
J^B j_{x,i}^{n+1/2} &= \frac{1}{\Delta t \Delta z} \sum_p \sum_\nu q_p v_{p,x}^{v+1/2} S_2\left(z_p^{\nu+1/2} - z_i\right) \Delta\tau_p^\nu, \\
J^B j_{y,i}^{n+1/2} &= \frac{1}{\Delta t \Delta z} \sum_p \sum_\nu q_p v_{p,y}^{\nu+1/2} S_2\left(z_p^{\nu+1/2} - z_i\right) \Delta\tau_p^\nu,
\end{aligned}
\tag{15}
$$

where S_1 and S_2 represent first and second order splines respectively. The wave magnetic field components might be computed with standard finite differences and scattered to particle positions similar to $\boldsymbol{E}$ or

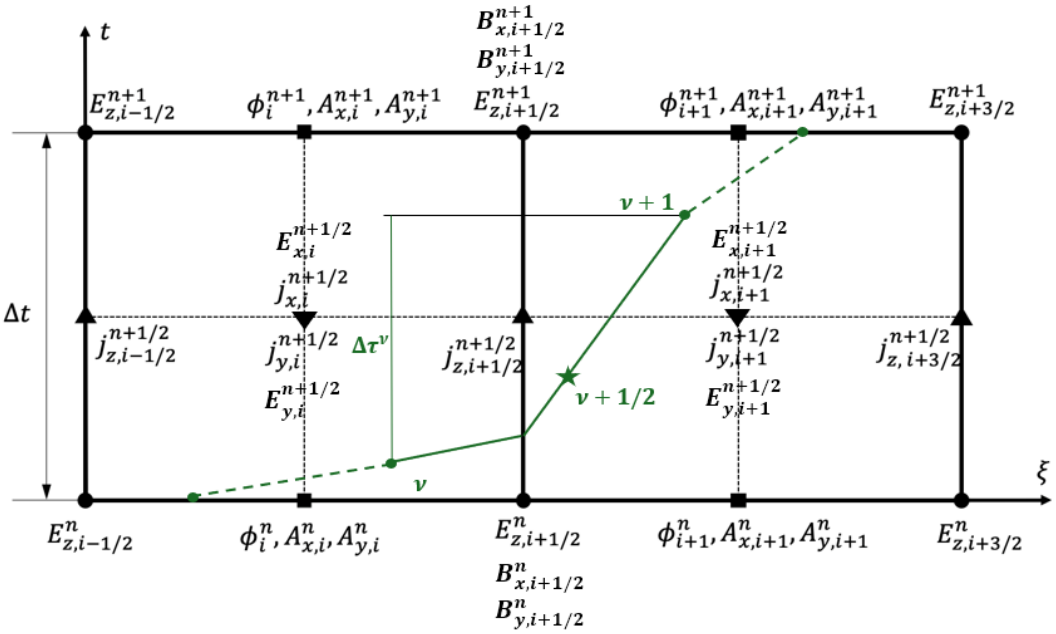

Figure 1. Diagram of the space-time simulation domain. All field quantities are shown at the positions where they are computed. A sample particle trajectory is displayed in green. One of the suborbits (solid green) crosses two cells, the space-time slope changes to reflect that the mesh map need not be uniform. The fields are interpolated to the particle position at mid-orbit $(\nu + 1/2)$**. Cells are uniform in logical space; the mesh map to physical space can be any smooth function** $z(\xi)$**.**

alternative expressions exist that ensure conservation of the system canonical moment [30].

After discretization, a coupled system of nonlinear algebraic equations must be solved. Given a guess of the particle particle coordinates at the new time step $\mathbf{X_2} = \{z^{n+1}, v_z^{n+1}, v_x^{n+1}, v_y^{n+1}\}_p$ and the scalar and vector potentials at the cell centers $\mathbf{X_1} = \{\phi_i^{n+1}, \boldsymbol{A}_i^{n+1}\}$, a nonlinear residual vector $\mathbf{F}(\mathbf{X_1}, \mathbf{X_2}) = 0$ can be formed and solved iteratively. The particle and field equations are coupled through the moments of the distribution function, in particular $\boldsymbol{j}$, required as sources into the field equations. As a result, this method results in an impractically large number of unknowns. To make the problem manageable, Chen et.al. [15] exploited the fact that the new particle coordinates depend on the potential, which allows us to express the residual as $\mathbf{F}_1(\mathbf{X}_1, \mathbf{f}_2(\mathbf{X}_1)) = \mathbf{G}(\mathbf{X}_1) = 0$. Finding $\mathbf{f}_2(\mathbf{X}_1)$ involves integrating the equations of motion for each particle, given the potentials on the cell centers $\mathbf{X_1}$, and accumulating the moments to form the residual vector $\mathbf{G}(\phi_i^{n+1}, \boldsymbol{A}_i^{n+1})$ from the field equations. This process, known as particle enslavement, allows a global nonlinear solver, such as the Jacobian Free Newton Krylov (JFNK) method, to handle a significantly reduced system of equations without compromising accuracy.

It can be shown that this numerical procedure ensures the conservation of global energy and local (per cell) charge [28] to nonlinear solver and machine roundoff error, respectively. Furthermore, the stability characteristics of the implcit PIC method have been studied in the literature [31] proving a stable algorithm and the absence of finite grid stabilities for cell sizes much larger than the local Debye length and timesteps much longer than the plasma period.

III. Magnetic nozzle simulations

In this section, we present the preliminary results of our study.

A. Simulation setup

The fundamentals of the simulation setup are similar to the one in [7]. Notably, the domain size has been expanded tenfold to allow for multiple R-wave wavelengths while maintaining the same relative magnetic field strength,

$$\boldsymbol{B}(z) = B_0 \frac{r_L^3}{\left(r_L^2 + z^2\right)^{3/2}} \mathbf{1}_z, \tag{16}$$

with $r_L = 0.012$ m and a magnetic field strength at the throat $B_0 = 0.096$ T. The domain is roughly 0.2 m long extending from $z = -0.5 r_L$ to $z = 16 r_L$. The magnetic topology creates a convergent, divergent nozzle with throat at $z = 0$. The plasma injection density and temperature are $n_e^* = 10^{18}$ m^{-3} and $T_e^* = 10$ eV. Electrons and ions are injected through the upstream end with equal temperatures $T_{\parallel e}^* = T_{\perp e}^* = T_{\parallel i}^* = T_{\perp i}^* = T_e^*$.

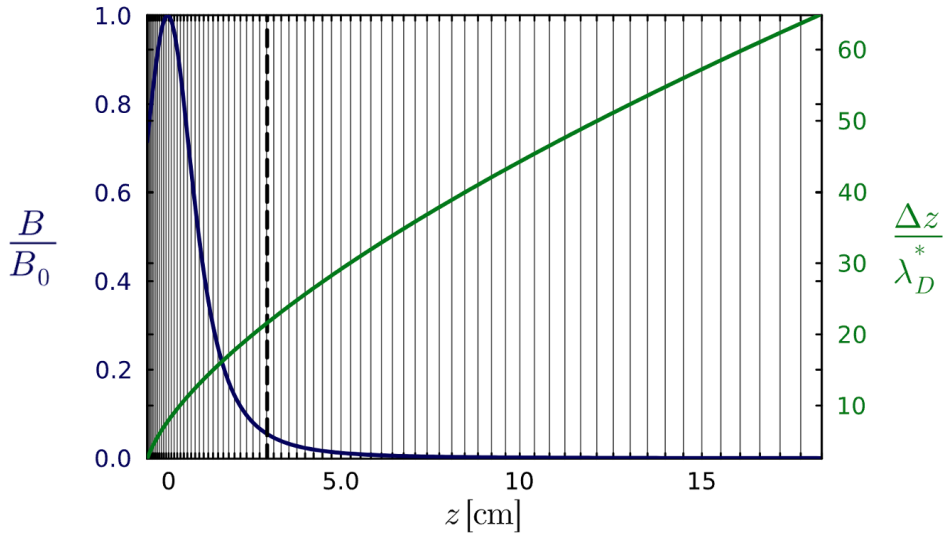

Figure 2. Relative magnetic field strength (left axis, blue) and local cell size over injection Debye length (right axis, green). The electron cyclotron resonance surface is depicted by a vertical black dashed line.

Figure 2 shows the simulation domain and the mesh employed. A nonuniform mesh is used, with the smallest cell size at the entrance $\Delta z = \lambda_D^*$, and much larger in the rarefied plasma downstream $\Delta z = 60\lambda_D^*$, where λ_D^* is the reference Debye length at injection. This mesh map adapts well to the most prominent potential gradients at the beginning of the domain and keeps the number of macroparticles per cell well balanced. The integration time step is $\Delta t = 2.5\ \omega_{pe}^{-1}$ and about 2 million macroparticles fill the domain in the steady state of all simulation cases.

A right-hand circularly polarized wave with frequency $f = \omega/2\pi = 2.6 \cdot 10^8$ Hz enters the domain from the upstream boundary. The domain displays an electron-cyclotron resonance (ECR) surface ($\omega_{ce} = \omega$) as the magnetic field decreases downstream the MN throat. Eventually, the plasma density is low enough to transition to an underdense regime ($\omega_{pe} < \omega$). In between these two critical transitions, the R-wave is known to become evanescent [32]. Consequently, we only expect a marginal fraction of the input power to tunnel downstream.

All parameters are physical with the exception of a reduced ion-to-electron mass ratio $m_i/m_e = 100$ (to keep the simulation comparable to previous works [7]), and a reduction in the speed of light constant by a factor 10. Contrary to many electromagnetic Vlasov-Maxwell algorithms, this reduction does not address any numerical concern related to fast wave propagation— because the Darwin approximation kills light speed traveling modes— but was merely introduced to decrease the characteristic wavelength $\lambda \propto d_e = c/\omega_{pe}$ and have several wavefronts inside the small simulation domain. A larger domain would involve much longer characteristic ion transit times and simulations. However, larger domains and realistic mass ratios (already demonstrated in [7]) are still well within the feasible limits of our model and are the objective of ongoing research beyond this preliminary study.

In the following, we study the results of different simulation cases:

- **Electrostatic case (ES)**: No wave is fed into the nozzle. The vector potential components are set to zero throughout the simulation domain $A_x = A_y = 0$. The domain is initially empty, a transient similar to the one reported in [7] takes place. This simulation is performed for reference and comparison, as well as to cross-verify with the previous 1D1V version of the code in that work (which assumed exact conservation of the magnetic moment μ rather than solving for v_x, v_y of the macroparticles).
- **Self-consistent electromagnetic cases (EM)**: We set the analytical vector potential corresponding to the R-wave as Dirichlet boundary condition in the upstream boundary $\{A_{x,0}(t),\ A_{y,0}(t)\}$ as explained in Section II.B. The vector potential and consequently the transverse electric field components evolve self-consistently according to the instantaneous plasma currents. We study two different power scenarios, **EM.high** with wave intensity (power per unit area) $I \sim 160$ W/cm^2, and **EM.low** where the wavefield amplitudes are halved and, as a consequence, the intensity is reduced by a factor of 4, $I \sim 40$ W/cm^2.
- **Imposed cold-plasma wavefields case (IW)**: Rather than solving self-consistently for the transverse fields, the cold-plasma-wave solution, described below, is prescribed in the whole domain. These fields are then used to move the particles. The analytical intensity of the incoming wave is $I = cn|E|^2/2 \sim 160$ W/cm^2, where n is the refractive index of the wave, similar to the **EM.high** case.

Each EM and IW case is initialized from the steady state of the ES case.

1. *Case IW: imposed fields*

The cold-plasma model is a widely used linear approximation for the propagation of electromagnetic waves through plasmas [32]. This model solves the full-Maxwell equations in the frequency domain and accounts for the linearized induced plasma currents. The main assumptions followed are to drop the thermal/pressure term in the electron-momentum equation and to keep only first-order terms in the plasma response, in the form of the anisotropic dielectric tensor $\boldsymbol{\kappa}$. The frequency domain second-order wave equation coming from the combination of Ampere's and Faradays' laws is:

$$\nabla \times (\nabla \times \hat{\boldsymbol{E}}) = -\nabla^2 \hat{\boldsymbol{E}} + \nabla(\nabla \cdot \hat{\boldsymbol{E}}) = \frac{\omega^2}{c^2} \boldsymbol{\kappa} \cdot \hat{\boldsymbol{E}}. \tag{17}$$

where ω is the wave frequency, and $\boldsymbol{E} = \hat{\boldsymbol{E}} \exp(-i\omega t)$. Following [33], we restrict this equation to a 1D domain with spatially-varying magnetic field and plasma density. We also assume that the effect of ions on wave propagation is small at ω, and keep only the electron contribution. Using the circular polarization basis, $\hat{\boldsymbol{E}}(z) = \hat{E}_R \mathbf{1}_R + \hat{E}_L \mathbf{1}_L$, where $\mathbf{1}_R = (\mathbf{1}_x + i\mathbf{1}_y)/\sqrt{2}$ and $\mathbf{1}_L = (\mathbf{1}_x - i\mathbf{1}_y)/\sqrt{2}$, we find the following uncoupled equation for E_R

$$\frac{\mathrm{d}^2 \hat{E}_R}{\mathrm{d}\zeta^2} + \left(1 + \frac{\eta}{\xi - i\gamma}\right) \hat{E}_R = 0 \tag{18}$$

where $\zeta = (\omega/c)z$, $\eta = (\omega_{pe}/\omega)^2$ and $\xi = \omega_{ce}/\omega - 1$. Finally, γ is a damping factor that captures collisional and kinetic wave damping in this fluid model. This factor (which could also be a function of z), is selected to match the kinetic results of the Darwin model presented in the next subsection.

This equation is solved for $\boldsymbol{E}_R(z,t) = \hat{\boldsymbol{E}}_R(z) \exp(-i\omega t)$ taking into account the applied magnetic field $\boldsymbol{B}_0$, and the steady-state plasma density profile from the ES case. The resulting field is imposed at each z an t, and particles are moved accordingly. To find solutions that correspond to power being injected only from the upstream side and not from the downstream side, uniform plasma regions are temporarily added upstream and downstream of the actual domain with the same properties as the first and last node, respectively, to facilitate the imposition of boundary conditions for the forward- and backward-traveling waves.

B. Stationary plasma profiles

Figure 3 shows the steady-state results, achieved after roughly 5000 plasma periods once the wave starts to be introduced through the upstream boundary. The profiles are depicted against the inverse of the magnetic field strength (increasing with z). The results are smoothed using a moving average with a window in time

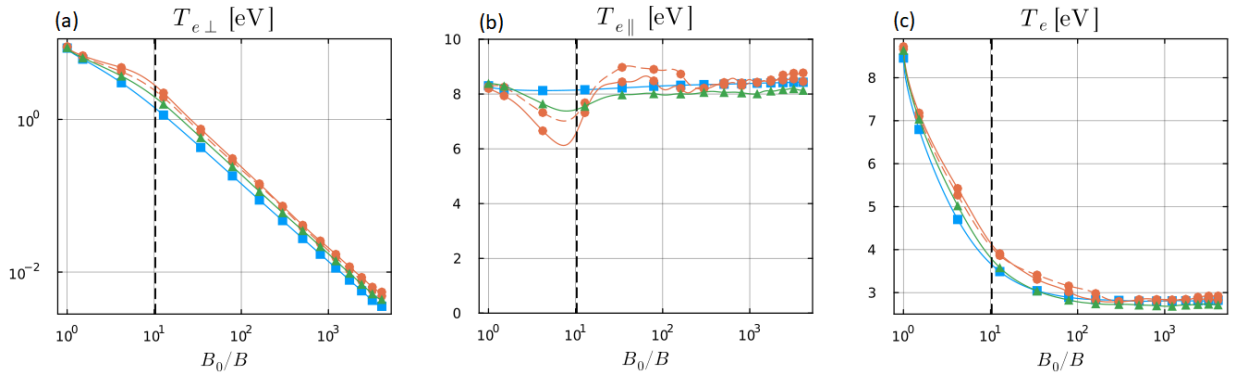

Figure 3. Steady state profiles of the electron perpendicular temperature (a), electron parallel temperature (b) and electron total temperature (c). Simulation cases ES (■), EM.low (▲), EM.high (● solid) and IW (● dash). The ECR surface is shown with a black dashed line.

of 500 ω_{pe}^{-1} to reduce PIC noise. Here we focus on the wave effects in the plasma expansion; for a general explanation of electrostatic magnetic nozzle mechanisms, refer to [34, 35, 7].

The effects of wave heating become evident when the perpendicular temperature in Figure 3.(a) is examined. In the ES scenario, the magnetic moment $\mu = m|v_\perp|^2/2B$ is exactly conserved, so that the electron perpendicular energy only responds to changes in the magnetic field strength. This can be observed in the almost linear decrease of $T_{\perp e}$ with $1/B$ for the ES line (blue). The magnetic mirror force acts behind this reduction, converting the perpendicular electron energy to axial. For the EM and IW cases, this behavior is modified before and in the resonance region, where an increase in $T_{\perp e}$ is remarkable. Heating is caused by the power transfer from the wave to the electrons, as further explained in Section III.C. However, downstream of the ECR, where the wave fields are negligible, the trend $T_{\perp e} \sim B_0^{-1}$ resumes.

Previous studies [35] and our reference ES case in Figure 3.(b) indicate that electrostatic magnetic nozzles tend to keep the electron parallel temperature fairly constant throughout the expansion. However, when the wave is activated, a different structure emerges. In the EM and IW cases, there is a significant drop of approximately 25% in the parallel temperature before the ECR, followed by a recovery downstream, ultimately reaching a level similar to that in the ES case. This phenomenon hints at a non-trivial evolution of the electron velocity distribution function (EVDF), which is inspected in section III.D. The total temperature $T_e = (2T_{e,\perp} + T_{e\parallel})/3$ in pane (d) is the consequence of the dynamics explained for the parallel and perpendicular ones, and is everywhere larger than in the ES case.

Overall, electron energy (directed and thermal) is increased by the interaction with the wave with respect to the energy available at injection, which is the sole source of energy in the ES case. Any electron perpendicular energy is converted into axial energy thanks to the magnetic mirror effect, as discussed before. This additional axial electron energy drives a larger drop in electrostatic potential as shown in Figure 4.(a). Ultimately, it is through the mediation of this electrostatic potential that the axial electron energy is converted into axial ion energy, leading to ion acceleration. This is clearly observed in Figure 4, where u_i and n_i are depicted. Their behaviors are the natural consequence of the profiles of ϕ and B_{z0} by virtue of $u_i \propto \sqrt{\phi}$ and the paraxial continuity equation $n_i u_i/B = \text{const}$. In the EM cases, a greater acceleration and a faster expansion is observed than in the ES case. The density distribution, in turn, is important for wave propagation, as it determines ω_{pe}. Nevertheless, the variations in density are minimal in this respect, particularly upstream of the ECR where the wavefields are most significant. This partially validates our use of the ES solution's density profile for wavefield calculations in the IW, rather than dynamically updating it as the density changes.

Concerning the variations among the simulation cases, although the wave intensity is comparable in the EM.high and IW cases, nearly all previously discussed profiles show that the IW lines fall between the EM.low and EM.high results. This suggests a lower power coupling in the IW case, which is corroborated by the power absorption plot shown in Figure 5.(c), as commented on in the next section.

Finally, in several of the previous figures, some minor spatial fluctuations are observed downstream. This could be due to these preliminary simulations not being fully converged to steady state; however, we observe some oscillating structures in the EVDF analysis of Section III.D, which could be causally linked to them.

Clarification of these fluctuations is object of ongoing research.

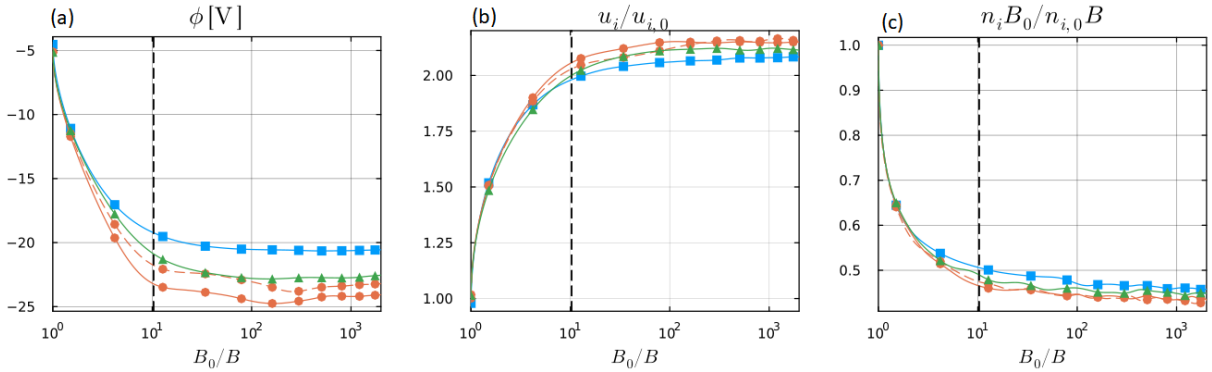

Figure 4. Electrostatic potential, normalized ion velocity and ion density over magnetic field strength. Simulation cases ES (■), EM.low (▲), EM.high (● solid) and IW (● dash). The ECR surface is shown with a black dashed line.

C. Transverse electric fields and power deposition

The transverse fields E_x and E_y are shown in Figure 5.(a). The incoming wave has a right-hand circular polarization as observed in the 90 deg phase difference between the fields. The fields are maximum and nearly constant in the region between the entrance and the throat, where they increase slightly, before being damped in a broad region up to the position of the resonance. The transfer of electromagnetic power to the plasma in this area is clearly observed in pane (b), the power absorption peaks just before the resonance position, but the deposition region is comparable to the fields wavelength. The absorption before the ECR surface could be caused by electrons resonating at different frequencies because of the Doppler effect. This effect is significant in our simulations because of the high thermal velocity over the speed of light caused by the artificial reduction of c. A similar behavior was observed by Porto et.al. [9]. The power per electron in pane (c) shows an even more remarkable deposition near the resonance driven by a reduction in density downstream. This figure is important because it determines the local changes in temperature discussed in Section III.B [24]. In both (b) and (c), there is a region of negative power transfer from the particles to the wave prior to the main heating peak. We anticipate that this might be caused by the synchronization of the particle gyro-phase with the transverse fields, but further inspection, e.g. exploring the evolution of individual particle orbits, is needed to understand this behavior.

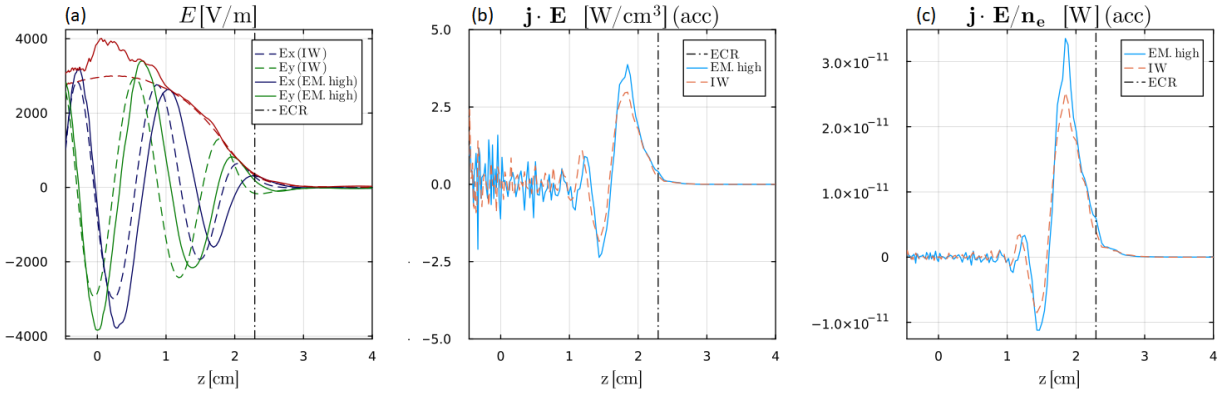

Figure 5. Transverse field E_x and E_y (a), power absorption (b) and power absorption per electron (c). Solid lines correspond to the EM.high case and dashed lines to the IW case.

The differences observed between the EM and IW fields in Figure 5. (a) are minor in both the amplitude and phase of the fields. The EM case seems to propagate with a slightly longer wavelength and its magnitude is larger in the throat region $z = 0$. The power deposition in panes (b) and (c) is qualitatively equivalent,

but the EM case shows a slightly higher deposition, notably near the ECR. This small mismatch was also confirmed by integrating the power deposition $\boldsymbol{j} \cdot \boldsymbol{E}$ and comparing it with the wave intensity.

The EM damping rate is successfully reproduced by the IW simulation after adjusting the parameter γ in the cold plasma model. The final value $\gamma = 0.5\omega$ is high compared to the usual collision frequencies in EPTs plume and sources [36]. This large value could be again attributed to the broadening of the heating region, in fact, Merino et al. [33] showed that the γ parameter fundamentally controls the width of this area, but not much the total power absorbed. These findings indicate that the Darwin approximation is valid in this regime, as it produces results comparable to the full Maxwell cold-plasma equation. Indeed computing a posteriori the missing $\partial^2 \boldsymbol{A}/\partial t^2$) term from our solution and comparing it against the $\boldsymbol{j}$ term shows that the former is 2–3 orders of magnitude smaller than the latter. Only very far downstream, where the plasma density is very low, does this term becomes comparable to the plasma currents. In fact, in this region the wave propagation regime approaches vacuum conditions, where the full-Maxwell equations are needed for the accurate simulation of the fields. However, as we will see in Section III.C, the transverse fields are almost negligible in that region.

Additionally, the good agreement between the kinetic-Darwin and the imposed-cold-plasma waves, by adjusting the collisional parameter, indicates that the cheaper cold-plasma model can be adequately tuned by means of kinetic simulations to accurately replicate the macroscopic aspects of wave propagation and damping of the latter. This hints at the interesting possibility of having a hierarchy of models, where the most complex/expensive ones are used to train/tune the simpler ones, achieving the best of both worlds.

D. Electron velocity distribution function

Figure 6 shows the steady-state electron velocity distribution function (EVDF) normalized by the density in each z cross section, and projected in various particle coordinates for the ES, EM.high, and IW simulation cases. In the electrostatic scenario (first column), the conservation of the magnetic moment μ (first row) per particle results in an almost uniform Maxwellian phase space distribution everywhere except near the throat, where particles with small μ become confined. In contrast, a noticeable increase in μ is seen between the throat and the ECR surface for the EM.high and IW cases (second and third columns), after which the normalized magnetic moment returns to its usual trend and remains nearly constant before the exit. Although nothing relevant is observed in the ES case, the gyrophase plots (second row) for the EM.high and IW cases show the presence of almost vertical strips of depleted or increased phase-space density that correlate well with half the wavelength of the R-wave. These structures are purportedly caused by the synchronization of particles in their gyro-orbits with transverse-wave fields.

The axial electron velocity is shown in the last row of Figure 6. In all cases, the distribution appears to be in general Maxwellian-like downstream of the initial ~ 5 cm but with an abrupt cut in the negative velocity half close to $v_z/v_{t,e} \sim 2$. This behavior is caused by the threshold energy in the downstream particle boundary conditions that reflects only the least energetic electrons. An interesting observation in cases EM and IW, is the formation of a structure of increased density around the position of an effective resonant surface $\omega_{eff} = \omega_{ce}$ where $\omega_{eff} = \omega - v_z k$ is the Doppler shifted wave frequency seen by the particles due to the non-negligible thermal speed over the wave phase velocity. This effective resonance line is represented by a black dashed line in the last row of Figure 6. Furthermore, the development region of the Doppler structure corresponds well to the decrease in parallel temperature in Figure 3.(b) and the negative power deposition area in Figure 5.(b). The precise cause of this behavior is not clear and may involve mediation of the mirror force and synchronization of particles and wave fields. In addition, we should bear in mind that the phase plots are the sum of different populations of electrons (free, reflected, and trapped) with notably different properties, as studied in previous works [7, 35].

The differences between EM.high and IW cases are, once again, minor and are mainly attributed to a lower power coupling in the IW case. The EM.high case features particles with higher perpendicular energy (and μ), and a more evident structure at the Doppler line. Certain downstream oscillations are more visible in the μ plot of the EM case. These could be related to the structures observed in Figures 3 and 4 and will be discussed in future work.

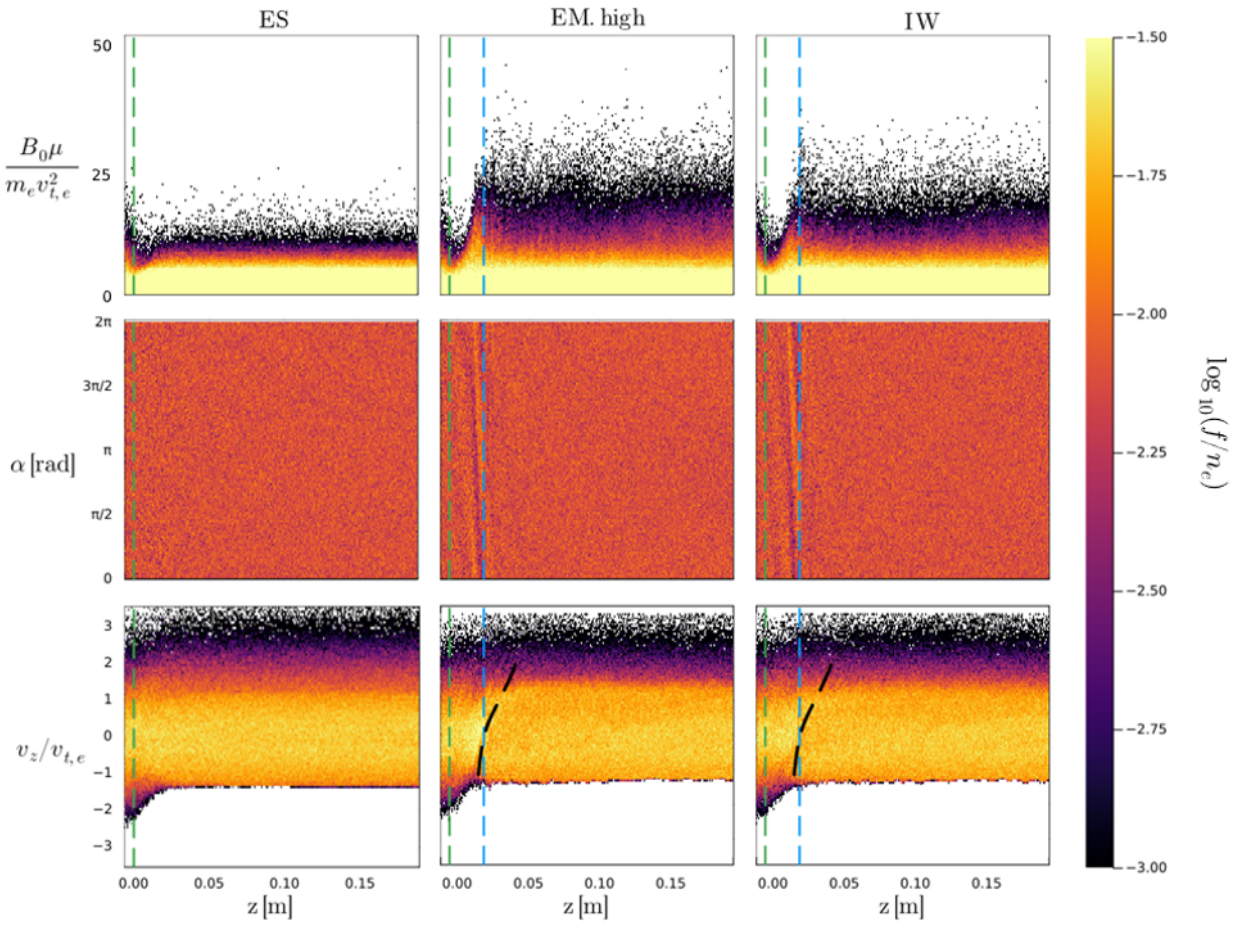

Figure 6. Phase space density of the electron velocity distribution function (EVDF) for different simulation cases. Magnetic moment μ (first row), gyrophase α (second row) and parallel velocity v_z (third row). The quantities are normalized with characteristic simulation values, particularly the thermal velocity of electrons at injection $v_{t,e}$. For a better visualization, the maps are divided by the electron density in each z cross section. The throat is depicted by a green dash vertical line while the ECR surface is depicted by a blue dashed line. The black dashed lines in the last row correspond to the effective Doppler shifted resonance surface.

IV. Discussion and conclusion

The study introduced a novel electromagnetic implicit PIC model for electric propulsion, enabling the investigation of various phenomena including the transfer of energy from electromagnetic waves to the perpendicular electron temperature, its impact on the electrostatic potential and ion acceleration, and the changes in the electron velocity distribution function, with observations such as the Doppler broadening in the ECR heating area.

In addition, the comparison of the electromagnetic kinetic simulations with the cold-plasma model showed similar wave propagation and absorption characteristics once the damping parameter is adjusted in the latter. This comparison partially validates both approaches and, in particular, the Darwin approximation to Maxwell's equations, which is nevertheless seen to be highly accurate in dense plasmas in our test case. Furthermore, the good agreement of the tuned cold-plasma wave model with the kinetic solution supports the valuable possibility of using the latter in fitting phenomenological parameters for reduced, faster models.

The performance of the method can be evaluated as follows. Our preliminary implementation is not optimized and is intended to demonstrate the ability of the algorithm to solve relevant plasma thruster problems. For comparison with other methods, we use a back-of-the-envelope estimate like the one in [30] on the computational savings of implicit Darwin electromagnetic algorithms vs. classical explicit methods.

That work shows the following CPU wall time ratio:

$$\frac{CPU_{exp}}{CPU_{imp}} \sim \frac{0.01}{(k\lambda_D)^d}\frac{c}{v_A}\min\left[\frac{1}{k\lambda_D}, \frac{c}{v_A}\sqrt{\frac{m_e}{m_i}}, \sqrt{\frac{m_i}{m_e}}\right]\frac{1}{N_{FE}} \tag{19}$$

where d is the physical space dimensionality of the problem, k is the characteristic wave number of the propagating fields, $v_a = B_0/\sqrt{\mu_0 m_0 n_0}$ is the Alfvén speed and N_{FE} is the number of times the particle's are moved before achieving convergence in the non-linear solver. For a plasma similar to the one studied before but using Xe mass ratio and the actual value of the speed of light, thus realistic plasma thruster conditions, speed-ups of order ~ 100 are obtained in 1D, ~ 2500 in 2D and ~ 60000 in 3D. This relies on maintaining good convergence and a bounded $N_{FE} \sim 10$, which has been demonstrated feasible in the past by Chen et.al. [20] by using appropriate preconditioning techniques (not implemented in this study). The estimate also assumes an essentially-quasineutral plasma domain, so fine sheath structures need not be captured. However, in the presence of Debye sheaths, non-uniform meshes and population control algorithms could help maintain the previous scaling. The notable computational gain figures justify the efforts toward building higher dimensional implicit PIC codes and applying them to realistic study cases.

We conclude that the implicit PIC scheme together with the Darwin approximation surpasses the performance of explicit PIC algorithms (and moreover so if the full Maxwell equations are implemented), while retaining accuracy and adding conservation properties. Future research will focus on employing realistic simulation parameters, specifically the speed of light constant and the ion-to-electron mass ratio, as well as the implementation of an optimized code version that can exploit the full potential of the algorithm.

Appendix A: Verification: Periodic Electron Weibel Instability

To further verify our implementation of the implicit PIC-Darwin model, we replicate the electron Weibel instability simulations conducted by Chen et al. [30], where additional details are available. In essence, the Weibel instability is an electromagnetic instability that arises in an unmagnetized plasma because of velocity-space anisotropy. When the plasma is hotter in the perpendicular direction, a perturbation in the magnetic field can generate a self-reinforcing plasma current that amplifies the original disturbance.

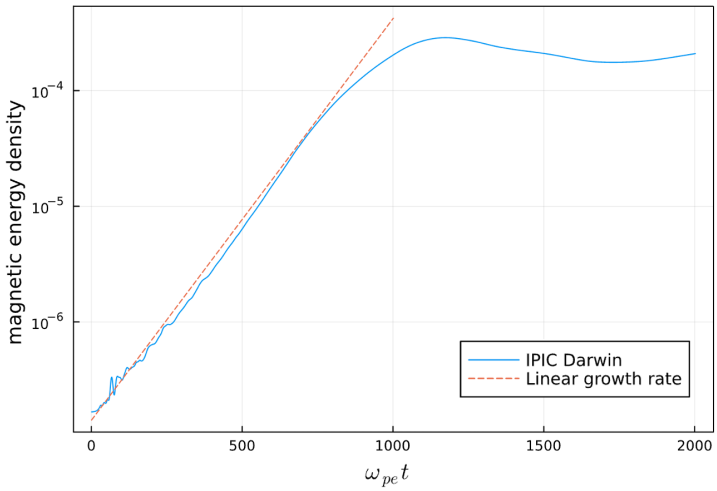

Figure 7. Numerical magnetic field energy and linear growth rate for the electron Weibel instability simulation.

We introduce one such perturbation in the perpendicular velocity $v_p = v_{p0} + a\cos(2\pi z/L)$, where $a \ll 1$. Electrons are sampled uniformly in the physical space from an anisotropic Maxwellian distribution with thermal velocity $v_{te} = \sqrt{T_{ez}/m_e} = 0.025c$ and $T_{e\perp}/T_{ez} = 2.56$. The ion distribution function is isotropic with $T_i = T_{ez}$. From linear theory, the solution of the dispersion relation [37] shows that the magnetic energy must evolve as $W_B = W_{B0}\exp(2\gamma\omega_{pe}t)$, where $\gamma = 0.004$ is the linear growth rate for the initial parameters introduced before.

The analytical results from linear theory and the numerical magnetic field energy computed by the implicit electromagnetic PIC, $W_{B,PIC} = \sum_i (B^2_{y,i+1/2} + B^2_{z,i+1/2})\Delta z/2$, are shown in Figure 7. In the

simulations, we use a uniform grid with $n_z = 64$ cells in a domain of $L = 32c/\omega_{pe}$ with periodic boundary conditions. About 8000 particle per cell are employed and a quiet-start procedure (Sobol sequence) is needed to prevent excessive noise in the initialization. An excellent match with the linear growth rate is observed up to saturation in Figure 7. The results also closely follow those of [30]. It has been checked that energy is conserved up to the non-linear tolerance of the JFNK solver and local charge to machine round-off error.

Acknowledgments

This project has received funding from the European Research Council (ERC) under the Horizon 2020 research and innovation program of the European Union (project ERC-StG ZARATHUSTRA, grant agreement No. 950466).

References

[1] Kazunori Takahashi, Christine Charles, Rod Boswell, and Akira Ando. "Performance improvement of a permanent magnet helicon plasma thruster". In: *Journal of Physics D: Applied Physics* 46.35 (2013), p. 352001.

[2] J Navarro-Cavallé, M Wijnen, P Fajardo, and E Ahedo. "Experimental Characterization of a 1 kW Helicon Plasma Thruster". In: *Vacuum* 149 (2018), pp. 69–73. DOI: 10.1016/j.vacuum.2017.11.036.

[3] Shunjiro Shinohara, Hiroyuki Nishida, Takao Tanikawa, Tohru Hada, Ikkoh Funaki, and Konstantin P Shamrai. "Development of electrodeless plasma thrusters with high-density helicon plasma sources". In: *IEEE Transactions on Plasma Science* 42.5 (2014), pp. 1245–1254.

[4] J.C. Sercel. "An experimental and theoretical study of the ECR plasma engine". PhD thesis. California Institute of Technology, 1993.

[5] Victor Désangles et al. "ECRA Thruster Advances: 30W and 200W Prototypes Latest Performances". In: *Journal of Electric Propulsion* 2.1 (2023), p. 10. DOI: 10.1007/s44205-023-00046-x.

[6] Marco Inchingolo, Jaume Navarro-Cavallé, and Mario Merino. "Design and Plume Characterization of a Low-Power Circular Waveguide Coupled ECR Thruster". In: *5th International Workshop on Micropropulsion and CubeSats*. Toulouse (online), 2021.

[7] Pedro Jiménez, Luis Chacón, and Mario Merino. "An implicit, conservative electrostatic particle-in-cell algorithm for paraxial magnetic nozzles". In: *Journal of Computational Physics* 502 (2024), p. 112826. DOI: https://doi.org/10.1016/j.jcp.2024.112826.

[8] A. Sánchez-Villar, J. Zhou, M. Merino, and E. Ahedo. "Coupled plasma transport and electromagnetic wave simulation of an ECR thruster". In: *Plasma Sources Science and Technology* 30.4 (2021), p. 045005. DOI: 10.1088/1361-6595/abde20.

[9] Jean Porto, Paul-Quentin Elias, and Andrea Ciardi. "Anisotropic electron heating in an electron cyclotron resonance thruster with magnetic nozzle". In: *Physics of Plasmas* 30.2 (2023).

[10] Filippo Cichocki, Jaume Navarro-Cavallé, Alberto Modesti, and Gonzalo Ramírez Vázquez. "Magnetic Nozzle and RPA Simulations vs. Experiments for a Helicon Plasma Thruster Plume". In: *Frontiers in Physics* 10 (2022). DOI: 10.3389/fphy.2022.876684.

[11] Shaun Andrews, Simone Di Fede, and Mirko Magarotto. "Fully kinetic model of plasma expansion in a magnetic nozzle". In: *Plasma Sources Science and Technology* (2022).

[12] Alberto Marín-Cebrián, Enrique Bello-Benítez, Adrián Domínguez-Vázquez, and Eduardo Ahedo. "Macroscopic response of a Hall thruster discharge from an axial-radial PIC model". In: 76th *Gaseous Electronics Conference*. Ann Arbor, MI, October 9-13, 2023.

[13] Johan Carlsson, Igor Kaganovich, Andrew Powis, Yevgeny Raitses, Ivan Romadanov, and Andrei Smolyakov. "Particle-in-cell simulations of anomalous transport in a Penning discharge". In: *Physics of Plasmas* 25.6 (2018). DOI: 10.1063/1.5017467. URL: https://doi.org/10.1063/1.5017467.

[14] C.K. Birdsall and A.B. Langdon. *Plasma Physics via Computer Simulation*. Bristol: Institute of Physics Publishing, 1991.

[15] Guangye Chen, Luis Chacón, and Daniel C Barnes. "An energy-and charge-conserving, implicit, electrostatic particle-in-cell algorithm". In: *Journal of Computational Physics* 230.18 (2011), pp. 7018–7036.

[16] Giovanni Lapenta. "Exactly energy conserving semi-implicit particle in cell formulation". In: *Journal of Computational Physics* 334 (2017), pp. 349–366.

[17] Guangye Chen and Luis Chacón. "An implicit, conservative and asymptotic-preserving electrostatic particle-in-cell algorithm for arbitrarily magnetized plasmas in uniform magnetic fields". In: *Journal of Computational Physics* 487 (2023), p. 112160.

[18] D Eremin et al. "Electron dynamics in planar radio frequency magnetron plasmas: II. Heating and energization mechanisms studied via a 2d3v particle-in-cell/Monte Carlo code". In: *Plasma Sources Science and Technology* 32.4 (2023), p. 045008.

[19] F. Taccogna, F. Cichocki, D. Eremin, G. Fubiani, and L. Garrigues. "Plasma propulsion modeling with particle-based algorithms". In: *Journal of Applied Physics* 134.15 (Oct. 2023), p. 150901. DOI: 10.1063/5.0153862. URL: https://doi.org/10.1063/5.0153862.

[20] Guangye Chen, Luis Chacón, Christopher A Leibs, Dana A Knoll, and William Taitano. "Fluid preconditioning for Newton–Krylov-based, fully implicit, electrostatic particle-in-cell simulations". In: *Journal of computational physics* 258 (2014), pp. 555–567.

[21] Guangye Chen and Luis Chacon. "A multi-dimensional, energy-and charge-conserving, nonlinearly implicit, electromagnetic Vlasov–Darwin particle-in-cell algorithm". In: *Computer Physics Communications* 197 (2015), pp. 73–87.

[22] Dennis W Hewett. "Elimination of electromagnetic radiation in plasma simulation: The Darwin or magneto inductive approximation". In: *Space Plasma Simulations: Proceedings of the Second International School for Space Simulations, Kapaa, Hawaii, February 4–15, 1985*. Springer. 1985, pp. 29–40.

[23] Todd B. Krause, A. Apte, and P.J. Morrison. "A unified approach to the Darwin approximation". In: *Physics of Plasmas* 14.10 (2007). DOI: 10.1063/1.2799346.

[24] Pedro Jiménez, Jiewei Zhou, Jaume Navarro-Cavallé, Pablo Fajardo, Mario Merino, and Eduardo Ahedo. "Analysis of a cusped helicon plasma thruster discharge". In: *Plasma Sources Science and Technology* 32.10 (2023), p. 105013. DOI: 10.1088/1361-6595/ad01da.

[25] Richard D Hazeltine and James D Meiss. *Plasma confinement*. Courier Corporation, 2003.

[26] Min Li, Mario Merino, Eduardo Ahedo, and Haibin Tang. "On electron boundary conditions in PIC plasma thruster plume simulations". In: *Plasma Sources Science and Technology* 28.03 (2019), p. 034004. DOI: 10.1088/1361-6595/ab0949.

[27] R.W. Hockney and J.W. Eastwood. *Computer simulation using particles*. CRC Press, Boca Ratón, FL, 1988.

[28] Luis Chacón and Guangye Chen. "A curvilinear, fully implicit, conservative electromagnetic PIC algorithm in multiple dimensions". In: *Journal of computational physics* 316 (2016), pp. 578–597.

[29] Long Chen et al. "Growth mechanism and characteristics of electron drift instability in Hall thruster with different propellant types". In: *Chinese Physics B* 33.1 (2024), p. 015203. DOI: 10.1088/1674-1056/acf9e5. URL: https://dx.doi.org/10.1088/1674-1056/acf9e5.

[30] Guangye Chen and Luis Chacón. "An energy-and charge-conserving, nonlinearly implicit, electromagnetic 1D-3V Vlasov–Darwin particle-in-cell algorithm". In: *Computer Physics Communications* 185.10 (2014), pp. 2391–2402.

[31] DC Barnes and Luis Chacón. "Finite spatial-grid effects in energy-conserving particle-in-cell algorithms". In: *Computer Physics Communications* 258 (2021), p. 107560.

[32] Thomas H Stix. *Waves in plasmas*. Springer Science & Business Media, 1992.

[33] Mario Merino et al. "Wave Propagation and Absorption in ECR Plasma Thrusters". In: 35^{th} *International Electric Propulsion Conference*. IEPC-2017-105. Atlanta, GA: Electric Rocket Propulsion Society, 2017.

[34] Mario Merino, Judit Nuez, and Eduardo Ahedo. "Fluid-kinetic model of a propulsive magnetic nozzle". In: *Plasma Sources Science and Technology* 30.11 (2021), p. 115006. DOI: 10.1088/1361-6595/ac2a0b.

[35] Gonzalo Sánchez-Arriaga, Jiewei Zhou, E Ahedo, Manuel Martínez-Sánchez, and Jesús José Ramos. "Kinetic features and non-stationary electron trapping in paraxial magnetic nozzles". In: *Plasma Sources Science and Technology* 27.3 (2018), p. 035002.

[36] Pedro Jiménez, Mario Merino, and Eduardo Ahedo. "Wave propagation and absorption in a Helicon plasma thruster source and its plume". In: *Plasma Sources Science and Technology* 31.4 (2022), p. 045009. DOI: 10.1088/1361-6595/ac5ecd.

[37] N.A. Krall and A.W. Trivelpiece. *Principles of Plasma Physics*. Ed. by McGraw-Hill. McGraw-Hill, 1973.